Vibrational properties of monoclinic $CoTeO_4$

P. Pramanik,[1,*] F. Eder,[2,3] M. Weil,[2] S. A. Ivanov,[1,4] P. Maltoni,[1,5,6] R. Miletich,[7] T. Edvinsson,[1,8] and R. Mathieu[1,†]

[1]*Department of Materials Science and Engineering, Uppsala University, Box 35, SE-75103 Uppsala, Sweden*

[2]*Institute for Chemical Technologies and Analytics, Division of Structural Chemistry, TU Wien, Getreidemarkt 9/E164-05-1, A-1060 Vienna, Austria*

[3]*Department of Quantum Matter Physics, Faculty of Sciences, University of Geneva, Quai Ernest-Ansermet 24, 1211 Geneva, Switzerland*

[4]*Department of Chemistry, M.V. Lomonosov Moscow State University, Leninskie Gory 1/3, Moscow 119991, Russia*

[5]*Università degli Studi di Genova, Dipartimento di Chimica e Chimica Industriale, nM2-Lab, Via Dodecaneso 31, 1–16146 Genova, Italy*

[6]*CNR, Istituto di Struttura della Materia, nM2-Lab, Monterotondo Scalo (Roma), 00015, Italy*

[7]*Institut für Mineralogie und Kristallographie, Universität Wien, Josef-Holaubek-Platz 2, A-1090 Vienna, Austria*

[8]*Energy Materials Laboratory, School of Natural and Environmental Science, Newcastle University, Newcastle Upon Tyne NE1 7RU, United Kingdom*

(Received 11 April 2024; revised 4 June 2024; accepted 26 July 2024; published 8 August 2024)

The vibrational properties of monoclinic dirutile-type $CoTeO_4$ (space group $P2_1/c$) were investigated by means of Raman and infrared (IR) spectroscopy on stoichiometric single crystals and theoretical density-functional theory (DFT) calculations. Experimental *in situ* investigations under pressure and temperature variations up to 10.1 GPa and 750 K confirmed the singular phase stability of the monoclinic lattice and the absence of any structural transition. The IR spectra exhibit modes that are not observed in the Raman spectra, thus offering a comprehensive understanding of the vibrational behavior of the title compound. The symmetry and degeneracy of modes and their contributions to the overall vibrational spectrum of $CoTeO_4$ were analyzed using group theory. DFT calculations were performed both on a cluster level and based on the crystal structure of monoclinic $CoTeO_4$ in order to gain further insights into the vibrational properties. The calculated vibrational frequencies and modes were compared with the experimental data, allowing for a detailed investigation of the lattice dynamics and the nature of the vibrational modes in $CoTeO_4$, and are corroborated with the analytical Wilson's F-G matrix method. These findings provide fundamental insights into the crystal symmetry and lattice dynamics of $CoTeO_4$. The results are discussed and compared to those of isoformular systems.

DOI: 10.1103/PhysRevB.110.054104

I. INTRODUCTION

Oxidotellurates (VI) of 3*d*-transition metals have been the subject of extensive research over the past few decades because of their fascinating physical properties and potential applications in energy sectors [1–11]. The physical properties and structural stability of scheelite-, wolframite-, and spinel-type ABO_3, A_3BO_6, ABO_4 and A_5BO_8 (A = 3*d* transition metal, B = Te) compounds are known to be influenced by the nature of constituent cations, especially through cationic ordering, octahedral distortion, and the distribution of the A and B cations throughout the octahedral or tetrahedral sites [1,3,12–16]. Furthermore, these materials have also recently gained importance as promising candidates for designing and developing modern optics components and for many other applications, such as energy storage and oxygen sensing [17–20]. Materials with both relevant magnetic and dielectric properties such as multiferroics are actively being investigated, owing to the possibility to design new spintronic devices, utilizing both magnetic and electronic polarizations or the magnetoelectric effects associated to their coupling [21]. In this context, the presence of magnetic cations in combination with highly polarizable ferroelectric active tellurium cation opens up many opportunities for the design of new multiferroics [22].

The most studied features of this family of materials are the magnetic structures and phase transitions of the transition-metal orthotellurates (VI) A_3TeO_6 (A = Mn, Co, and Ni). For example, monoclinic (space group $C2/c$) cobalt orthotellurate Co_3TeO_6 emerged as an interesting type II multiferroic material that shows antiferromagnetic (AFM) order at low temperatures together with complex and temperature-dependent spin structures [22–25]. Hudl *et al.* also reported the magnetic-field-driven electric polarization of Co_3TeO_6 at low temperatures, indicating the existence of strong coupling between magnetic and electric dipole orders [22]. Mn_3TeO_6 exhibits AFM order below 24 K and a multiferroic ground state below 21 K together with incommensurate cycloidal

*Contact author: prativa9piitg@gmail.com

†Contact author: roland.mathieu@angstrom.uu.se

and helical spin structures [26,27]. Ni_3TeO_6, in contrast to its isoformular Co-compound, exhibits a collinear AFM order [28], yet with magnetically induced polarization effects akin to those observed in Co_3TeO_6 [29].

In the case of $ATeO_4$ (A = Co, Ni) with its dirutile type structure, the existing literature is limited and highly contradictory, although $CoTeO_4$ was reported to be an antiferromagnet below $T_N = 50$ K, albeit with no consensus on the crystal structure [8–10]. Whereas Isasi reported the crystal structure of $CoTeO_4$ as monoclinic (space group $P2_1/n$) structure, Sikač and Jenšovský reported the crystal structure to follow cubic symmetry [9,10]. Most recently, Weil *et al.* confirmed the monoclinic symmetry (space group $P2_1/c$), however with a different crystal structure than that reported by Isasi [30].

Inelastic Raman scattering has become a robust and simple technique to probe local structure and group symmetries through phonon dynamics. Together with systematic pressure- and temperature-dependent Raman investigation, we present here the crystal structure and some remarkable aspects of the phase stability in $CoTeO_4$, which are crucial to elucidate the lattice dynamics. There is only one earlier publication dealing with the vibrational characteristics of $CoTeO_4$, and the assignment and detailed analysis of vibrational modes have not yet been disclosed [9]. This paper reports the results of a joint experimental and ab initio study of the electronic structure and vibrational properties of $CoTeO_4$ in order to understand the nature of the metal-oxygen coordination and the structural homogeneity. A comparison with isoformular materials is made, which in turn facilitates mode assignments and a detailed analysis of both the first- and second-order scattering.

II. METHODS

A. Experimental details

Euhedral single crystals of $CoTeO_4$ were grown from polycrystalline material (prepared from a stoichiometric mixture of H_6TeO_6 and $Co(NO_3)_2(H_2O)_6$ using chemical vapor transport reactions [30]. Room temperature powder x-ray diffraction confirmed the phase purity and the monoclinic crystal structure of $CoTeO_4$, space group $P2_1/c$ (14) with lattice parameters $a = 5.5635(12)$ Å, $b = 4.6675(10)$ Å, $c = 5.5424(12)$ Å, $\beta = 112.321\,°(6)$ [30] (and the Supplemental Materials of [30]). The oxygen content was determined to be close to stoichiometric (3.991(6)), by iodometric titration. Energy dispersive x-ray spectroscopy confirm equimolar stoichiometric amounts of Co and Te and the x-ray photoelectron spectroscopy measurements indicate oxidation states of +II and +VI for Co and Te, respectively [30]. The vibrational characteristics of $CoTeO_4$ single crystals were analyzed by infrared (IR) and Raman spectroscopy at ambient conditions. A Perkin-Elmer Fourier transform spectrophotometer was used to measure the mid-IR spectra in the range 400–1000 cm^{-1} through reflectance mode. The infrared reflectance spectrum was recorded at a resolution of 2 cm^{-1}. Raman spectroscopy was measured using a multichannel bench Renishaw InVia Reflex spectrometer coupled with 1024-pixel Rencam CCD detector and 2400 lines per millimeter grating and a 20x and 50x objective to focus both the incident laser beam into a spot down to 1–2 μm in diameter and collect the scattered light in backward-scattering geometry. The Raman shift was recorded with 532-nm green and 785-nm red laser in a broad range of wave number (100 to 1000 cm^{-1}) using a spectral resolution of 1 cm^{-1} per detection pixel [31]. Different excitation wavelengths imply different scattering intensities and sensitivity, and usable laser powers. The scanning parameter for each Raman spectrum was fixed to 1 s exposure time to lower the laser heating, while 100 scans were instead accumulated for each experimental run-in order to get better signal-to-noise ratio. Multiple scans on different areas of the same sample were performed with lower laser power to ensure spectral reproducibility. We measured 100% laser power equivalent to 40 and 48 mW at the sample's surface for 785 nm and 532 nm excitation wavelength, respectively, using a Thorlabs PM160T power meter. Percentages of the full power was typically used in the measurements; the laser power employed in each experiment is indicated in the figures showing Raman spectroscopy data. Each batch of measurements were calibrated with a standard Si reference line of 520.5 cm^{-1}. For *in situ* high pressure investigations, a selected euhedral single crystal of $CoTeO_4$ was mounted with its morphologically dominant face onto one of the culet faces using an *ETH*-type [32] diamond-anvil cells equipped with Böhler Almax-type [33] type-I diamond anvils (C = 0.6 mm). The pressure chamber was prepared from stainless steel gaskets preindented to ∼100 μm thickness with a borehole of 250 μm in diameter. Cryogenically loaded dense argon was used as pressure-transmitting medium considering the given hydrostatic limits [34]. Pressures were determined using a conventional laser-induced ruby luminescence standard [35], applying the calibration according to [36]. Uncertainties of pressure determination account to within ±0.05 GPa as obtained from the R_1-line shift of the ruby luminescence signal. The initial pressure after cryogenic loading was found to be 8.19 GPa. Compression was achieved in four steps up to 10.15 GPa, with subsequent decompression to ambient pressure in steps of approximately 1 GPa. At each step, a Raman spectrum of the sample and the reference crystal was measured using a red He-Ne laser operated at 20 mW at a wavelength of 632.8 nm. A series of high-pressure Raman spectra were recorded with the same orientation of the polarization vector of the incident laser beam relative to the given arbitrary position of the crystal specimen within the pressure chamber, without knowing exactly the actual crystallographic orientation. Details of the instrumental settings of the *in situ* measurements are provided in the Supplemental Material [37].

B. Computational details

Density functional theory (DFT) was performed on two levels to support the experimental findings. In a first set of calculations, idealized clusters with octahedral symmetry (O_h) were performed using Gaussian 09 [39], and complementary crystal state calculations using Crystal 17 [40]. In both cases, the structures were first optimized to the lowest ground state energy using 10^{-10} Hartree convergence criteria. The linear response calculations were utilized as implemented in the codes, with a small perturbation of the positions in the ground

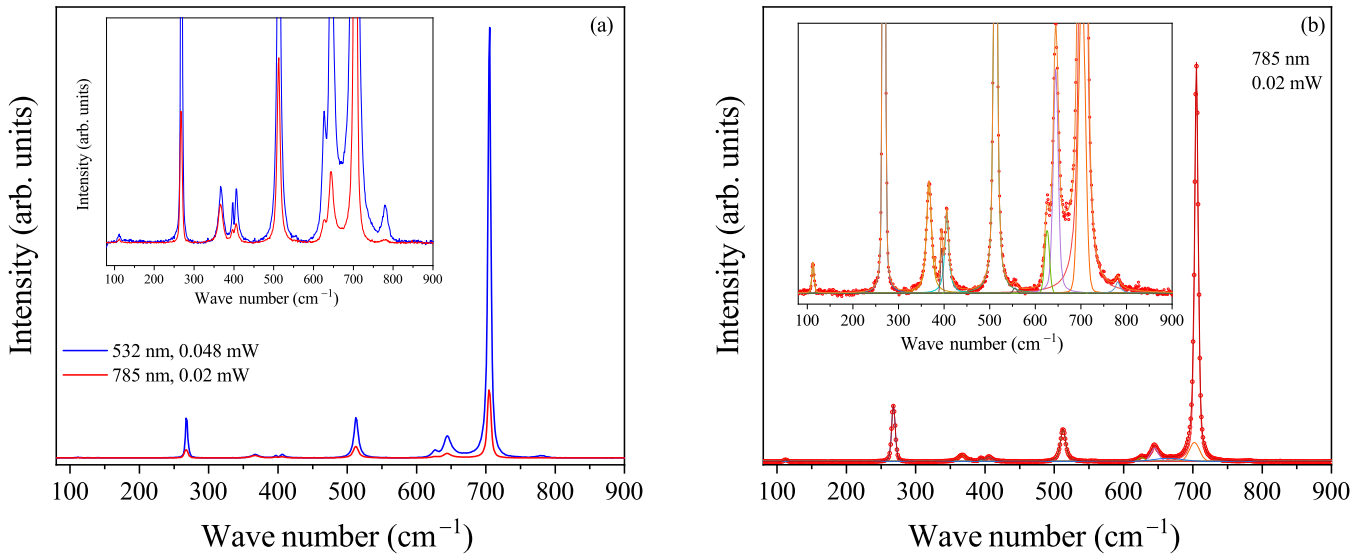

FIG. 1. (a) Comparison of Raman scattering spectra of $CoTeO_4$ SC with different laser excitation after background corrections. (b) Fitted curve with the Pseudo-Voigt profile. Inset figures show extended view for clear understanding.

state structures to obtain the interatomic forces and extraction of the change in polarizability, and subsequently extracting the theoretical Raman response. For the cluster calculations and the ideal tetrahedral TeO_4 structure unit we benchmarked the Perdew-Burke-Ernzerhof (PBE), Becke, 3-parameter Lee–Yang–Parr (B3LYP), Coulomb-attenuating method B3LYP, and HSE: Heyd-Scuseria-Ernzerhof (HSE06) functionals, at a 6–311(d,p) level with experimental match for the PBE and HSE06 functionals, where the latter was utilized for calculations for the ideal tetrahedral TeO_4, and octahedral TeO_6 clusters, while also keeping track of the results for PBE. To calculate the crystal structure of $CoTeO_4$, we employed a PBE functional with $8 \times 8 \times 8$ k points and a 10^{-10} Hartree convergence criteria, two orders of magnitude lower than the typical value for electronic structure calculations as the forces, as the Raman response depend on the second derivative of the nuclei position and are much more sensitive to a tight conversion criterion.

III. RESULTS AND DISCUSSIONS

A. Raman spectroscopy

Figure 1(a) shows the Raman spectrum of $CoTeO_4$ single crystal, measured at 532- and 785-nm laser excitation wavelengths of 0.048 and 0.02 mW power, respectively. Very sharp and symmetrical peaks present in both spectra at this low laser power indicate the high-quality crystallinity of the sample. A zoomed view of the less intense peaks is presented in the inset. The identical patterns of Raman spectra obtained with both lasers indicate that the phonon frequencies of this sample are independent of the excitation wavelength, for wavelengths above 532 nm. Figure 1(b) presents the fitted Raman spectrum with pseudo-Voigt function and indicates a total of twelve vibrational modes, of which 704.6 cm^{-1} is the most intense band. Only a small percentage of Gaussians (5–8%) were included with the Lorentzians in the pseudo-Voigt functions, which in practice renders them to be mainly Lorentzians. The inclusion of a small portion of Gaussians is not affecting the peak position analysis, and only improve the overall peak shape fitting. In Table I, the observed Raman shifts in wave numbers ($\bar{\nu}_{expt}$ (cm^{-1})) are listed, along with their fitting parameters such as intensity, full width at half maxima (FWHM) and the theoretically obtained ($\bar{\nu}_{Theory}$ (cm^{-1})) mode frequency.

The reproducibility of the present study was confirmed by recording several spectra from different crystals. Figures 2(a) and 3(a) show the Raman spectra collected with 785- and 532-nm lasers of different powers. Similarly, Figs. 2(b) and 3(b) present various Raman spectra collected from different locations on the surface of the sample. Figure 1(a) was found to be reproducible, except one or two data out of thirty spectra shows additional modes at 663 and 223 cm^{-1}, marked with * in the Table I. These additional modes may arise due to

TABLE I. Comparison of observed phonon frequencies (cm^{-1}) from Raman scattering (resolution ±1 cm^{-1}) with the theoretical results, and their force constant. Additional modes are marked with *.

$\bar{\nu}_{expt}$(cm^{-1})	Intensity	FWHM	Force constant (Nm^{-1})	$\bar{\nu}_{Theory}$ (cm^{-1})
780.3	215.09	6.00		609.7 (B_g)
704.6	117481.9	3.13	509	608.2 (A_g)
663*				
643.7	4148.94	6.54	6.7	528.8 (A_g)
626.9	1166.92	6.21	8	502.4 (B_g)
551	99.11	4.55		481.7 (A_g)
512.4	10015.91	4.85		485.0 (B_g)
405.5,	1515.32	4.99		456.4 (B_g)
396.7	858.94	2.63		425.7 (A_g)
366.4	2046.95	6.56	29.5	304.6 (B_g)
267.2	17353.26	3.09		198.9 (A_g)
223*				192.7 (B_g)
112	572.27	2.96		86.7 (A_g)

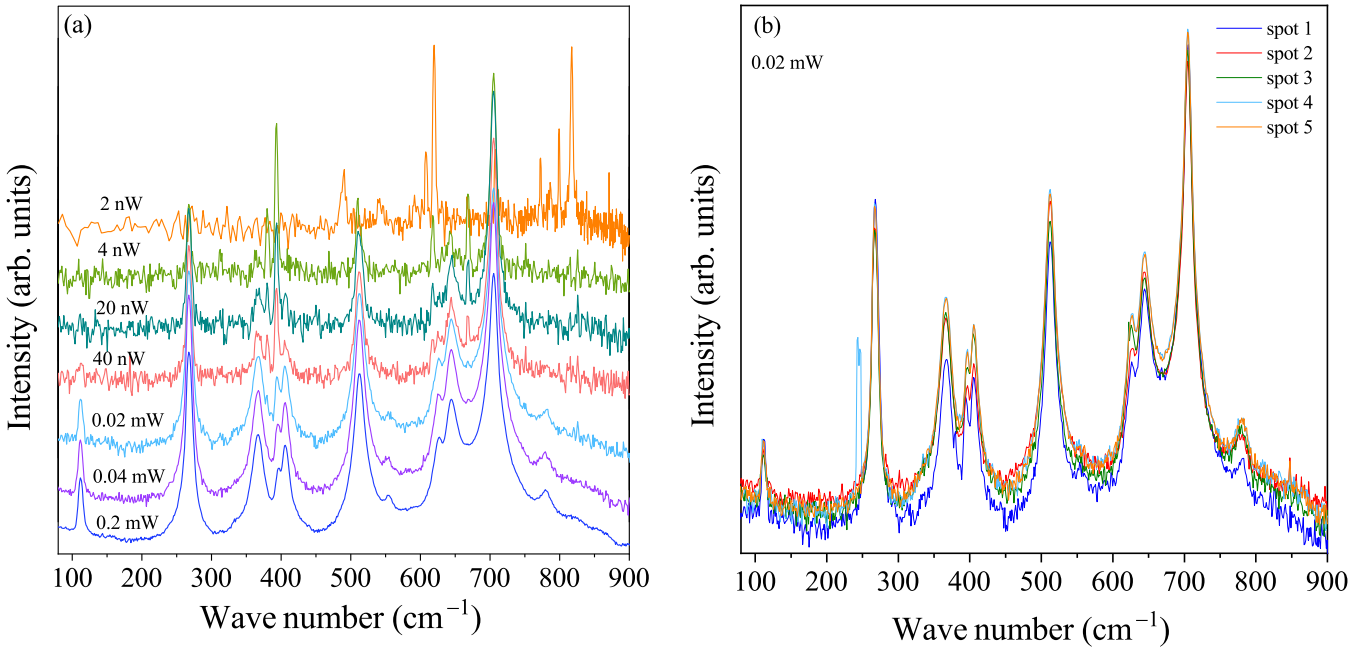

FIG. 2. Raman spectra with 785 nm excitation wavelength (a) using different laser power and (b) at different spots on the surface of SC.

small amounts of defects or distortions present in the crystal structure. Detailed discussions on mode assignments based on theoretical results are presented below. The Raman spectra of $CoTeO_4$ recorded under high laser power exposure are shown in Fig. 3(a), along with those of tellurium dioxide (TeO_2) and paratellurite (α-TeO_2) from the RRuff database [41], in order to verify the sample's purity and to examine the effects of laser power on the oxidation state of the metal cations. Tellurium is typically found in oxide compounds called tellurites and tellurates, respectively, having a +IV or +VI charge. According to literature, tellurates may easily be converted into tellurites by losing oxygen, typically for temperatures between 350° and 600 °C. Tellurites, on the other hand, are the most stable phases at room temperature. It is clear from Fig. 3(a) that when the laser power increases from 0.24 to 4.8 mW, the local heating modifies the cations' oxidation state and results in the appearance of additional Raman peaks. Therefore, for in-depth analysis only very low power have been used in this work to collect Raman spectra.

Pressure- and temperature-dependent Raman spectra were recorded in a series of individual data points in order to follow the spectral evolution with respect to any structural instability (see Supplemental Material). Figure SM2 (a) show the Raman spectra of $CoTeO_4$ at hydrostatic pressures up to 10.08 GPa and Fig. SM2 (b, c, d) correspondingly represent the Raman shift as a function of pressure for individual

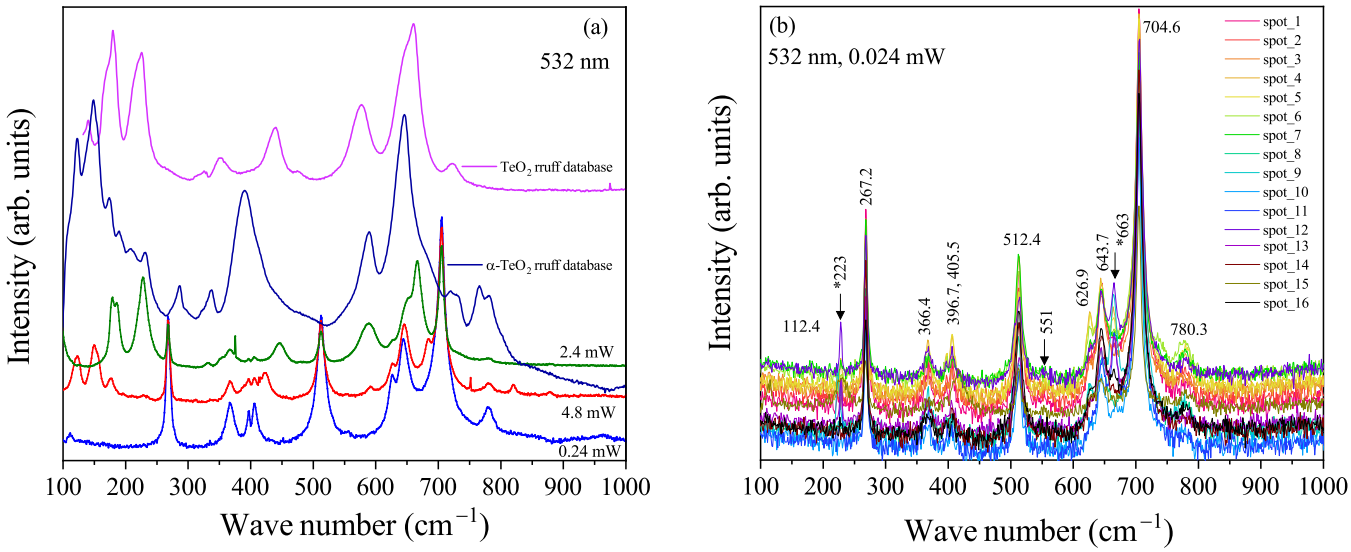

FIG. 3. Raman spectra with 532 nm excitation wavelength (a) using different laser power and (b) at different spots on the surface of SC. Some of the spectra show additional modes, which are identified with *; see main text and Table I.

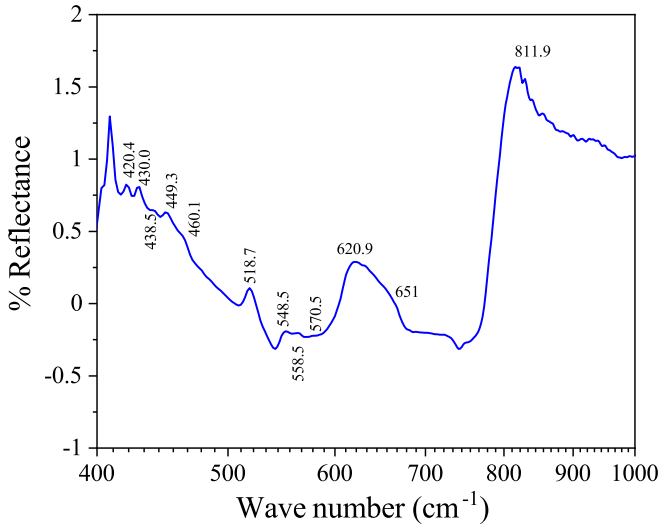

FIG. 4. Fourier transformed infrared spectrum of $CoTeO_4$ SC under reflectance mode.

TABLE II. Comparison of observed phonon frequencies (cm^{-1}) from FTIR spectroscopy with the theoretical results.

$\bar{\nu}_{expt}$ (cm^{-1}) IR	$\bar{\nu}_{Theory}$ (cm^{-1}) IR
812	
621, 651	
558, 570	562.8 (A_u)
548	556.9 (B_u)
518.7	509.06 (A_u), 496.04 (B_u)
438.5, 449.3, 460.1	469 (A_u), 455.8 (B_u), 449.4 (A_u)
430	433.9 (B_u)
420	
	337.1 (A_u), 336.6 (B_u)
	279 (B_u), 264 (A_u), 249.3 (A_u), 219.1 (B_u), 219.0 (A_u), 216.8 (B_u)
	179.5 (B_u), 176.8 (A_u), 165.7 (A_u), 150.6 (B_u), 121.4 (A_u)

modes. Neither any additional new bands, nor significant variations of the relative peak intensities or any observable peak splitting were observed from measurements, thus indicating singular phase stability up to the maximum pressure achieved. Complementary Raman measurements were performed as a function of temperature in the range of 300–750 K in heating cooling cycles [Fig. SM3 (a)] with temperature steps of 50 K and a waiting period of ten minutes to attain stable sample temperature before acquiring the spectrum. The individual peak shifts with temperature [Fig. SM3 (b, c, d)] also suggest the stability of the studied phase within the temperature range of experimental investigations, in agreement with recent temperature-dependent synchrotron measurements and thermal analyses [30].

B. Infrared spectroscopy

The Fourier-transformed infrared spectra of a $CoTeO_4$ single crystal are shown in Fig. 4 are plotted as percentage of reflectance versus wave number in cm^{-1}. Twelve reflectance modes were observed. Similar infrared spectra of cobalt tellurates were reported by Sikač and Jenšovský with only five modes. The authors considered the sample to belong to the cubic crystal system [9], while the lower symmetry, as relevant to the occurrence of a monoclinic structure, is expected to have a higher number of different bond lengths and thus an increased number of distinct vibration frequencies. The results of IR active vibrational modes and the theoretical results are summarized in Table II. A detailed discussion on symmetry considerations of these modes is presented in the next section.

C. Group theory and mode assignments

The unit cell of $CoTeO_4$ (shown in Fig. 5) belongs to C_{2h} ($2/m$) point group and consists of two formula units where the Co, Te and O (O_I, and O_{II}) atoms are located at the 2 a, 2 d and 4 e sites, respectively. According to group-theoretical analysis, $CoTeO_4$ has 36 vibrational modes at the center of the Brillouin zone: $6A_g + 6B_g + 12A_u + 12B_u$, here g and u represent Raman and IR active modes, respectively. Letters A and B characterize these modes as the symmetric and asymmetric vibrations. In addition, group-theoretical analysis suggests that Raman vibrations in $CoTeO_4$ are mainly related to the O motion while all cations are essentially at rest, and therefore there will be no cationic mass effect on vibration bands. Accordingly, we observe a total of 11 Raman modes from Fig. 1 at 780.3, 704.6, 643.7, 626.9, 551, 512.4, 405.5, 396.7, 366.4, 267.2, and 112 cm^{-1}. The number of observed vibrations is in good agreement with the group-theoretical predictions. These modes are mainly distributed into two ranges: (i) the high-wave number (>500 cm^{-1}), and (ii) the mid–wave number ($200 \leqslant \upsilon \leqslant 400$ cm^{-1}) range, which can be distinguished as internal and external vibrations of TeO_6 and CoO_6 blocks, by comparing the metal-oxygen bond strength following reference [12]. Liegeois-Duyckaerts and Tarte assigned the internal vibrations (highest wave number) of a complex system containing two or more cations (X^{6+}, Y^{2+}, Z^{4+} etc.) depending on the bond (X−O) strengths [12]. In a comparable manner, the highest wave numbers observed for $CoTeO_4$ at 780.3 and

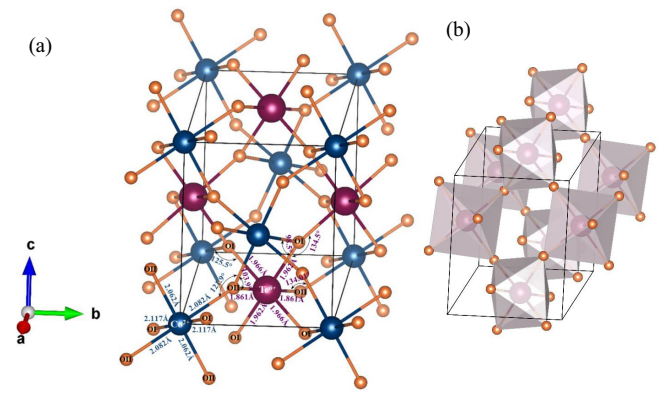

FIG. 5. (a) Crystal structure of $CoTeO_4$ at room temperature. Bond lengths and bond angles of corner-sharing CoO_6 (blue) and TeO_6 (wine) octahedra are presented in Å and °, respectively [30]. (b) Three-dimensional layers of TeO_6.

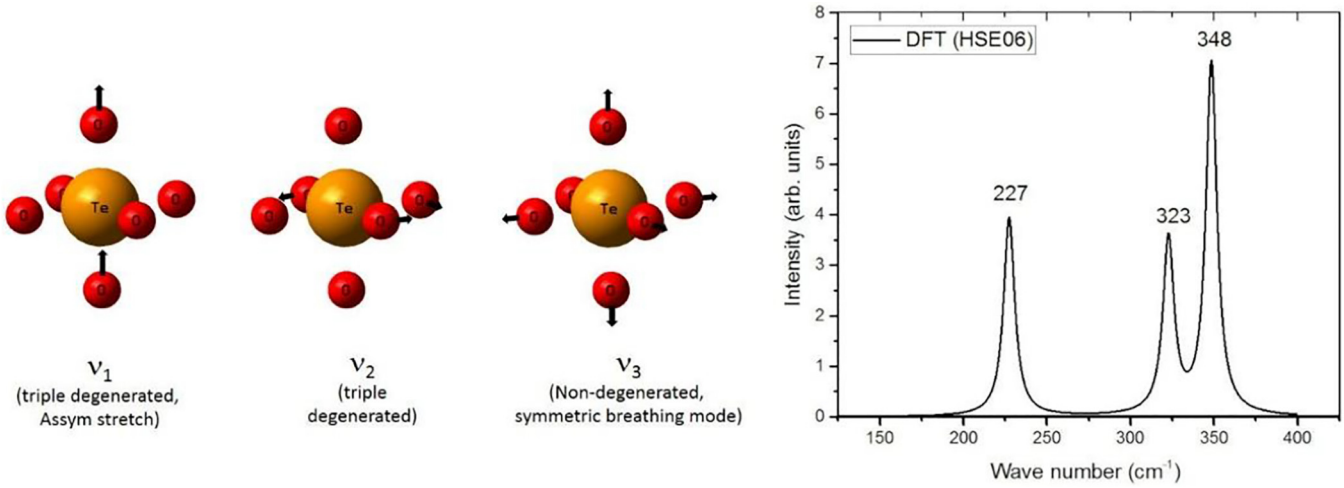

FIG. 6. Calculated Raman active vibration modes of TeO_6 clusters using the HSE06 hybrid functional.

704.6 cm^{-1} can be considered to originate from the motion of O atoms along Te−O or Co−O terminal bonds. On the other hand, the lower limits of high wave numbers at 643.7, 626.9, 551, and 512.4 cm^{-1} appear from the vibrations of O atoms along the bridge axis (Te−O−Te or Te−O−Co or Co−O−Co). The external vibrations or middle wave numbers at 405.5, 396.7, 366.4, 267.2, and 112 cm^{-1} arise in the Raman spectrum due to the bending motion of O atoms along O−Co−O, or O−Te−O. Further, these wave numbers are also associated with symmetric (*A*) and asymmetric (*B*) motions of oxygen atoms. Due to the lack of a preferential orientation of the crystals as suggested by the rather similar angular dependent spectrum (as shown in Fig. SM1), it is important to discuss the symmetric and asymmetric natures of these modes by recalling the crystal structure and comparing with isoformular compounds.

Figure 5 shows the unit cell of $CoTeO_4$ created using VESTA [42], where O^{2-} anions and Co, Te metal cations are located at 4 *e* (*x*, *y*, *z*), 2 *a* (0, 0, 0), and 2 *d* (0.5, 0, 0.5) Wyckoff positions, respectively [30]; both Te and Co atoms are surrounded by six neighboring oxygen atoms (O_I and O_{II}), linked by sharing faces and vertices. The shortest (degenerated) bonds Te−O_{II} (1.861 Å) are shared with four CoO_6 units, which results in symmetric Te−O_{II}−Co bridges with an angle of 134 °. Similarly, four other equivalent long Te−O_I (1.966 Å, and 1.962 Å) bonds connected with four TeO_6 and four CoO_6 octahedra are forming symmetric Te−O_{II}−Te and asymmetric Te−O_{II}−Co bridges with angles of 134 ° and 98 °, respectively. The average bond length of TeO_6 and CoO_6 is 1.92 and 2.087 Å, respectively.

In view of the structural complexity, we shall first limit ourselves to a general assignment of the internal modes by considering the chemical aspect of valence bonds. The smaller average bond length (1.92 Å) and ionic radius (0.56 Å) makes the octahedral bonding of TeO_6 stronger than that of CoO_6 (2.087 and 0.745 Å) [43], suggesting that the observed highest wave number peaks at 780.3 and 704.6 cm^{-1} are the internal vibrations of TeO_6 only. Alternatively, according to Badger's empirical formula the vibrational frequencies are inversely proportional to the 3/2 power of bond lengths, which also confirms the highest wave numbers to belong to TeO_6 [44]. The experimentally observed vibrational modes are compared to the theoretically obtained values in Table I. In the low-wave number region, the experimentally observed and the calculated Raman modes are in good agreement [45], while the high wave number modes seem too soft by 13−22%. This discrepancy can be ascribed to the following reasons: (i) the calculations use the average bond lengths, while three different bond lengths are present in the crystal structure as observed from x-ray crystallography; (ii) the effects of orbital splitting from the magnetic Co^{2+} cations result in deviations from an ideal isotropic system. Similar discrepancies between experimental and theoretical results of vibrational properties have previously been found in other complex low-symmetric samples [46–49]. Apart from predicted frequency from calculations, the ordering and relative intensity of the modes are important for assignment.

To establish an ideal behavior, we have calculated the fundamental modes of an isolated TeO_6 octahedron using the HSE06 functional form to identify and assign the internal vibrations. The TeO_6 octahedra belong to the O_h point group, for which group theory predicts three υ_1, υ_2, and υ_3 Raman active modes, corresponding to symmetric stretching, antisymmetric stretching and symmetric bending of octahedron. Figure 6 represents three fundamental modes at 348 (υ_1), 323 (υ_2) and 227 (υ_3) cm^{-1} for such a TeO_6 octahedron. The same approach was performed to calculate the fundamental modes of CoO_6 octahedra, but the calculations did not converge reliably without a charge-compensating matrix, but are generally in another range compared to the TeO_6 octahedron. The observed high wave numbers are attributed to TeO_6 units in the matrix instead. From the analysis of the displacement vectors from the theoretical calculations, the highest intense peak at 704.6 cm^{-1} can be assigned to the first overtone of the fundamental modes (υ_1) of TeO_6 where the O atoms symmetrically stretch along the terminal bonds (Te−O) and it belong to the A_g symmetry. The 780.3 cm^{-1} wave number is the third overtone of the υ_3 where the O atoms moves asymmetrically along the Te−O bonds, which are assigned as B_g. Similarly, 643.7 and 626.9 cm^{-1} modes observed in Fig. 1

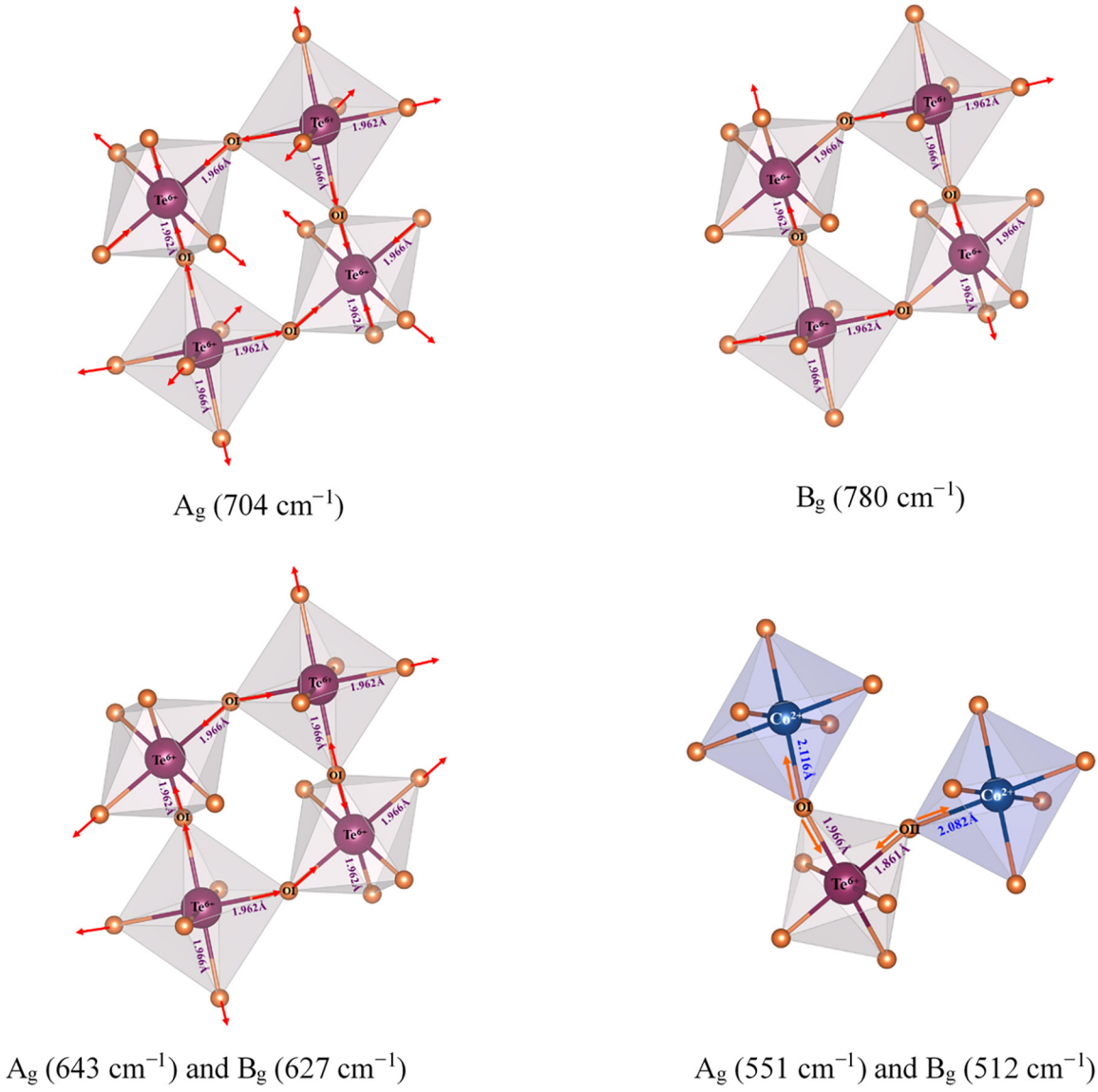

FIG. 7. Diagrams of Raman active phonon modes.

are the first overtones of υ_2 (323 cm^{-1}), where the O atoms move along Te−O−Te symmetrically and asymmetrically, respectively. By using VESTA, an illustrative representation of these vibrations with corresponding displacement vectors are presented in Fig. 7. Such high intense characteristic overtone peak near 700 cm^{-1} is also reported in several complex systems with octahedrally coordinated Te such as $BaTe_2O_6$, $Cs_4Te_4O_{12}$, $Ba_2R_{2/3}TeO_6$, A_2BTeO_6, and A_3TeO_6 [2,3,6,7,50–52]. The Raman modes that appear at 551, and 512.4 cm^{-1} due to symmetric and asymmetric modulation of O atoms along Te−O_{II}−Co are assigned as A_g and B_g, respectively.

A comparison of vibrational modes of $CoTeO_4$ with other $A^{2+}B^{6+}O_4$ compounds having different structures is presented in Table III. It is interesting to see that the higher wave numbers can be correlated to the $B^{6+}-O$ bond and can thus be used for detailed analysis of the local coordination. The higher range of middle wave numbers at 405.5 and 396.7 cm^{-1} is due to bending motions of O atoms along the Te−O_{II}−Te bridge, which makes an angle of 134 °. The 366.4 cm^{-1} band appear due to Te−O_{II}−Co bridges which make an angle of 98 °. Similarly, the lower wave numbers at 267.2 and 112 cm^{-1} are due to O movement along the Co−O_{II}−Co bridge with an angle of 121 °.

Furthermore, we carried out a detailed analysis of the vibrational modes in addition to the DFT computations. Here, the force constants of the observed vibrational frequencies were determined using the Wilson's F-G matrix method using the symmetry coordinates [53]. Using the Te−O bond lengths, we obtained the force constants for TeO_6, which are presented in Table I. The force constant values are comparable with TeF_6 [54].

D. Discussions of IR

The IR active bands are those that exhibit change in dipole moments during vibrational modes that can be excited by infrared radiation in a crystal. To understand the occurrence

TABLE III. Phonon frequencies (in cm^{-1}) of ABO_4 compounds. Mode symmetry or intensity (W: weak; M: medium; S: strong; V: very) is indicated in parentheses.

$CoTeO_4$	$CoWO_4$	$MnWO_4$	$CdWO_4$	$ZnWO_4$	α-$CoMoO_4$	$GeCo_2O_4$	CoO
[This work]	[55]	[56]	[57]	[58]	[59]	[60]	[61]
780.3 (W)	881 (A_g)	885 (A_g)	897 (A_g)	909 (A_g)	938		
					915		
704.6 (VS)	765 (B_g)	774 (B_g)	771 (B_g)	788 (B_g)	880	760 (A_{1g})	
643.7 (M)	686 (A_g)	698 (A_g)	707 (A_g)	711 (A_g)	815	647 ($T_{2g}(1)$)	690
626.9 (W)	657 (B_g)	674 (B_g)	688 (B_g)	680 (B_g)			
551 (VVW)	530 (A_g)	545 (A_g)	546 (A_g)	546 (A_g)	740	550 ($T_{2g}(2)$)	540
512.4 (M)	496 (B_g)	512 (B_g)	514 (B_g)	516 (B_g)	715		
					700		
405.5 (M)	403 (A_g)	397 (A_g)	388 (A_g)	409 (A_g)	476		
396.7 (VW)					440		
					429		
366.4 (M)	332 (A_g)	356 (B_g)	352 (B_g)	356 (B_g)	390		
	315 (B_g)				362		
	271 (B_g)	327 (A_g)	306 (A_g)	343 (A_g)	330	308 (E_g)	
				316 (B_g)			
267.2 (M)	199 (B_g)	258 (A_g)	269 (B_g)	276 (A_g)	286		
		272 (B_g)	249 (B_g)	269 (B_g)			
		294 (B_g)					
	182 (B_g)	206 (A_g)	229 (A_g)		193		
	154 (B_g)	177 (B_g)	177 (A_g)	196 (A_g)	155		
		166 (B_g)	148 (B_g)	191 (B_g)			
		160 (B_g)		166 (B_g)			
	125 (A_g)	129 (A_g)	134 (B_g)	147 (B_g)	130		
			118 (B_g)	124 (A_g)			
			100 (A_g)				
112.4 (B_g) (W)	88 (B_g)	89 (B_g)	78 (B_g)	93 (B_g)			

of IR active bonds in a monoclinic lattice, we need to consider the crystal's symmetry properties and its point group. The point group of a monoclinic crystal is typically denoted as C1 or C2, indicating a single or twofold rotational axis, respectively, along with other symmetry elements such as a mirror plane or inversion center. $CoTeO_4$, belongs to C1 with a mirror plane that divides the crystal into two identical halves. This plane is perpendicular to the unique axis (b axis) of the crystal and is the defining symmetry element of the monoclinic system. In addition, there is an inversion center, representing a point in the crystal from which each atom has an equidistant opposite. Since Raman and IR spectroscopy probe vibrations when the polarizability and dipole change during the atomic movement, and that they cannot both be active in a system with an inversion center, their combination allows for a more comprehensive analysis of the vibrational modes present. In a system with an inversion center, Raman spectroscopy will be sensitive to vibrations that transform symmetric with respect to the inversion center (Ag modes), making the system Raman active. On the other hand, IR spectroscopy will probe vibrations that transform antisymmetric with respect to the inversion center, making the system IR active. This allows for the characterization of different types of vibrations in molecules based on their symmetry properties.

DFT calculations were utilized to clarify the crystal IR-active phonon modes in the monoclinic $CoTeO_4$ and aiding in their assignment. Phonons represent the quantized lattice vibrations, and are here extracted by solving the dynamical matrix equations within the framework of hybrid DFT. These calculations provide information about the vibrational frequencies, eigenvectors, and mode symmetries. As $CoTeO_4$ has an inversion center, the optical phonons cannot be both Raman and IR-active (See Table ST1 for a full list of calculated phonon modes and their symmetries). As the experimental IR spectrum is in the range of $400-1000\,cm^{-1}$, we discuss these whereas calculated IR-active modes below 400 cm^{-1} can be found in the Supplemental Material. There are five IR-active phonon modes between 400 and 500 cm^{-1}, at 434, 449, 456, 469, and 496 cm^{-1} in relatively good agreement with the experimental detected modes (Table II, typically within $10-20\,cm^{-1}$). The experimental data, however, have broad peaks and developed shoulders, making an exact mode analysis from experimental data challenging. In the range $500-600\,cm^{-1}$, the experimental data show three modes, 519, 549, and 559 cm^{-1}, in good agreement with the theoretical vibrations at 509, 557, and 563 cm^{-1}. (Note that the peak in the experimental IR-figure at 570.5 cm^{-1}, is barely visible and cannot be faithfully assigned as a peak if we should be consistent with other features not assigned, such as the small peaks around the dip at 750 cm^{-1}.) The experimental data also show peaks beyond 600 cm^{-1}, with features at 621, 651, and 812 cm^{-1}, where no fundamental IR-active modes beyond 600 can be found from the theoretic assessment and are thus second-order Raman modes from overtones and combination modes.

IV. CONCLUSION

In this work, we have reported comprehensive lattice dynamics of stoichiometric $CoTeO_4$ single crystals based on Raman and infrared measurements and made an assignment of the experimentally observed bands to definite atomic vibrations based on the symmetry considerations of monoclinic structures. Furthermore, we have carried out *ab initio* lattice dynamic calculations for $CoTeO_4$ and our computed mode frequencies match the observed Raman modes' frequencies, enabling the modes' nature to be discussed and assigned. The impact of the divalent cation on the Raman frequencies is explored, and a methodical comparison of the experimental data amongst isoformular families is provided. We compute the stretching frequencies and the corresponding force constants for the TeO_6 group given in Table I by using the bond lengths obtained from the x-ray analysis. The variation of the different Raman frequencies has been analyzed as a function of temperature and pressure. It was shown to remain almost constant in the range from 0 to 10.08 GPa pressure as well as up to a very high temperature of 750 K which is clearly confirm singular phase stability. This analysis of the vibrational behavior of $CoTeO_4$ advances our understanding of its structural and functional characteristics.

ACKNOWLEDGMENTS

P.P. and R.M. thank Stiftelsen Olle Engkvist Byggmästare (Grant No. 207–0427) for financial support, and T.E. acknowledge the Swedish Research Council (Grant No. 2019–05591 and 2023–05244). The authors acknowledge Sofija Miloš for her technical assistance to record the *in situ* high-pressure Raman spectra. Research conducted by S.A.I. was carried out with the financial support of the Russian Science Foundation (Grant No. 22–13–00122).

[1] M. Liegeois-Duyckaerts, Vibrational studies of molybdates, tungstates and related compounds—IV. Hexagonal perovskites: $Ba_2B_{II}TeO_6$ (B_{II} = Ni, Co, Zn), Spectrochim Acta A **31**, 1585 (1975).

[2] D. Hamani, A. Mirgorodsky, O. Masson, T. Merle-Méjean, M. Colas, M. Smirnov, and P. Thomas, Crystal chemistry peculiarities of $Cs_2Te_4O_{12}$, J. Solid State Chem. **184**, 637 (2011).

[3] D. Hamani, A. Plat, M. Colas, J. Cornette, O. Masson, A. P. Mirgorodsky, and P. Thomas, Origin of the strong optical nonlinearity of tellurium oxide–based compounds: The specific case of $BaTe_2O_6$, J. Alloys Compd. **661**, 92 (2016).

[4] F. Eder, M. Weil, O. P. Missen, U. Kolitsch, and E. Libowitzky, The family of $M^{II}_3(Te^{IV}O_3)_2(OH)_2$ (M = Mg, Mn, Co, Ni) compounds—prone to inclusion of foreign components into large hexagonal channels, Crystals (Basel) **12**, 1380 (2022).

[5] R. L. Frost and E. C. Keeffe, Raman spectroscopic study of kuranakhite $PbMn^{4+}Te^{6+}O_6$–a rare tellurate mineral, J. Raman Spectrosc. **40**, 249 (2009).

[6] J. Qu, L. Yan, H. Liu, Q. Tao, P. Zhu, Z. Li, and X. Wang, Pressure-induced structural phase transition in corundum-related class Cu_3TeO_6, High Pressure Res. **41**, 318 (2021).

[7] L. Liu, H. Skogby, S. Ivanov, M. Weil, R. Mathieu, and P. Lazor, Bandgap engineering in Mn_3TeO_6: Giant irreversible bandgap reduction triggered by pressure, Chem. Commun. **55**, 12000 (2019).

[8] A. K. Patel, M. R. Panda, E. Rani, H. Singh, S. S. Samatham, A. Nagendra, S. N. Jha, D. Bhattacharyya, K. G. Suresh, and S. Mitra, Unique structure-induced magnetic and electrochemical activity in nanostructured transition metal tellurates $Co_{1-x}Ni_xTeO_4$(x = 0, 0.5, and 1), ACS Appl. Energy Mater. **3**, 9436 (2020).

[9] J. Sikač and L. Jenšovský, The preparation and properties of cobalt(II) tellurates, Collect Czechoslov. Chem. Commun. **45**, 2489 (1980).

[10] J. Isasi, New $MM'O_4$ Oxides derived from the rutile type: Synthesis, structure and study of magnetic and electronic properties, J. Alloys Compd. **322**, 89 (2001).

[11] S. J. Sondarva and D. V. Shah, Electrical properties of Mn_3TeO_6 multiferroic compound, Mater. Today Proc. **47**, 711 (2021).

[12] M. Liegeois-Duyckaerts and P. Tarte, Vibrational studies of molybdates, tungstates and related c compounds—III. Ordered cubic perovskites $A_2B_{II}B_{VI}O_6$, Spectrochim. Acta Part A **30**, 1771 (1974).

[13] M. Liegeois-Duyckaerts, Spectroscopic and structural studies of the hexagonal perovskite Ba_2CoTeO_6, Spectrochim Acta A **41**, 523 (1985).

[14] S. Smaoui, W. Ben Aribia, A. Kabadou, and M. Abdelmouleh, X-ray powder diffraction, spectroscopic study, dielectric properties and thermal analysis of new doped compound $TiGa_{0.67}Te_{2.33}O_8$, J. Mol. Struct. **1133**, 422 (2017).

[15] W. H. Li, C. W. Wang, D. Hsu, C. H. Lee, C. M. Wu, C. C. Chou, H. D. Yang, Y. Zhao, S. Chang, J. W. Lynn, and H. Berger, Interplay between the magnetic and electric degrees of freedom in multiferroic Co_3TeO_6, Phys. Rev. B **85**, 094431 (2012).

[16] S. Podchezertsev, N. Barrier, A. Pautrat, E. Suard, M. Retuerto, J. A. Alonso, M. T. Fernández-Díaz, and J. Rodríguez-Carvajal, Influence of polymorphism on the magnetic properties of Co_5TeO_8 spinel, Inorg. Chem. **60**, 13990 (2021).

[17] V. B. Voloshinov, K. B. Yushkov, and B. B. J. Linde, Improvement in performance of a TeO_2 acousto-optic imaging spectrometer, J. Opt. A **9**, 341 (2007).

[18] M. Soulis, J. R. Duclère, T. Hayakawa, V. Couderc, M. Dutreilh-Colas, and P. Thomas, Second harmonic generation induced by optical poling in new TeO_2-Ti_2O-ZnO glasses, Mater. Res. Bull. **45**, 551 (2010).

[19] J. H. Yuan, K. H. Xue, J. Wang, and X. Miao, Designing stable 2D materials solely from VIA elements, Appl. Phys. Lett. **119**, 223101 (2021).

[20] J. Fernández-Catalá, H. Singh, S. Wang, H. Huhtinen, P. Paturi, Y. Bai, and W. Cao, Hydrothermal synthesis of Ni_3TeO_6 and Cu_3TeO_6 nanostructures for magnetic and photoconductivity applications, ACS Appl Nano Mater **6**, 4887 (2023).

[21] N. A. Spaldin and R. Ramesh, Advances in magnetoelectric multiferroics, Nat. Mater. **18**, 203 (2019).

[22] M. Hudl, R. Mathieu, S. A. Ivanov, M. Weil, V. Carolus, T. Lottermoser, M. Fiebig, Y. Tokunaga, Y. Taguchi, Y. Tokura, and P. Nordblad, Complex magnetism and

magnetic-field-driven electrical polarization of Co_3TeO_6, Phys. Rev. B **84**, 180404 (2011).

[23] C. H. Lee, C. W. Wang, Y. Zhao, W. H. Li, J. W. Lynn, A. B. Harris, K. Rule, H. D. Yang, and H. Berger, Complex magnetic incommensurability and electronic charge transfer through the ferroelectric transition in multiferroic Co_3TeO_6, Sci. Rep. **7**, 6437 (2017).

[24] C. W. Wang, C. H. Lee, C. Y. Li, C. M. Wu, W. H. Li, C. C. Chou, H. D. Yang, J. W. Lynn, Q. Huang, A. B. Harris, and H. Berger, Complex magnetic couplings in Co_3TeO_6, Phys. Rev. B **88**, 184427 (2013).

[25] J. L. Her, C. C. Chou, Y. H. Matsuda, K. Kindo, H. Berger, K. F. Tseng, C. W. Wang, W. H. Li, and H. D. Yang, Magnetic phase diagram of the antiferromagnetic cobalt tellurate Co_3TeO_6, Phys. Rev. B **84**, 235123 (2011).

[26] S. A. Ivanov, P. Nordblad, R. Mathieu, R. Tellgren, C. Ritter, N. V. Golubko, E. D. Politova, and M. Weil, New type of incommensurate magnetic ordering in Mn_3TeO_6, Mater. Res. Bull. **46**, 1870 (2011).

[27] L. Zhao, Z. Hu, C. Y. Kuo, T. W. Pi, M. K. Wu, L. H. Tjeng, and A. C. Komarek, Mn_3TeO_6 – a new multiferroic material with two magnetic substructures, Phys. Status Solidi (RRL) **9**, 730 (2015).

[28] S. A. Ivanov, R. Mathieu, P. Nordblad, R. Tellgren, C. Ritter, E. Politova, G. Kaleva, A. Mosunov, S. Stefanovich, and M. Weil, Spin and dipole ordering in Ni_2InSbO_6 and Ni_2ScSbO_6 with corundum-related structure, Chem. Mater. **25**, 935 (2013).

[29] Y. S. Oh, S. Artyukhin, J. J. Yang, V. Zapf, J. W. Kim, D. Vanderbilt, and S. W. Cheong, Non-hysteretic colossal magnetoelectricity in a collinear antiferromagnet, Nat. Commun. **5**, 3201 (2014).

[30] M. Weil, P. Pramanik, P. Maltoni, R. Clulow, A. Rydh, M. Wildner, P. Blaha, G. King, S. A. Ivanov, R. Mathieu, and H. Singh, $CoTeO_4$ – a wide-bandgap material adopting the dirutile structure type, Mater. Adv. **5**, 3001 (2024).

[31] J. Thyr and T. Edvinsson, Evading the illusions: Identification of false peaks in micro-raman spectroscopy and guidelines for scientific best practice, Angew. Chem. Int. Ed. **62**, e202219047 (2023).

[32] R. Miletich, D. R. Allan, and W. F. Kuhs, High-pressure single-crystal techniques, Rev. Mineral. Geochem. **41**, 445 (2000).

[33] R. Boehler and K. De Hantsetters, New anvil designs in diamond-cells, High Press Res **24**, 391 (2004).

[34] R. J. Angel, M. Bujak, J. Zhao, G. D. Gatta, and S. D. Jacobsen, Effective hydrostatic limits of pressure media for high-pressure crystallographic studies, J. Appl. Crystallogr. **40**, 26 (2007).

[35] J. C. Chervin, B. Canny, and M. Mancinelli, Ruby-spheres as pressure gauge for optically transparent high pressure cells, Int. J. High Press. Res. **21**, 305 (2001).

[36] S. D. Jacobsen, C. M. Holl, K. A. Adams, R. A. Fischer, E. S. Martin, C. R. Bina, J. F. Lin, V. B. Prakapenka, A. Kubo, and P. Dera, Compression of single-crystal magnesium oxide to 118 GPa and a ruby pressure gauge for helium pressure media, Am. Mineral. **93**, 1823 (2008).

[37] See Supplemental Material at http://link.aps.org/supplemental/10.1103/PhysRevB.110.054104 for additional Raman spectroscopy data (polarized; pressure-dependent; temperature-dependent) and DFT results and which includes Ref. [38].

[38] M. Wojdyr, Fityk: A general-purpose peak fitting program, J. Appl. Crystallogr. **43**, 1126 (2010).

[39] M. J. E. A. Frisch, GAUSSIAN09 (Gaussian Inc., Wallingford, CT, 2009).

[40] R. Dovesi, A. Erba, R. Orlando, C. M. Zicovich-Wilson, B. Civalleri, L. Maschio, M. Rérat, S. Casassa, J. Baima, S. Salustro, and B. Kirtman, Quantum-mechanical condensed matter simulations with CRYSTAL, Wiley Interdiscip. Rev. Comput. Mol. Sci. **8**, e1360 (2018).

[41] B. Lafuente, R. T. Downs, H. Yang, and N. Stone, The power of databases: The RRUFF project, in *Highlights in Mineralogical Crystallography*, edited By T. Armbruster and R. M. Danisi (De Gruyter, Berlin, 2016), pp. 1–30.

[42] K. Momma and F. Izumi, VESTA3 for three-dimensional visualization of crystal, volumetric and morphology data, J. Appl. Crystallogr. **44**, 1272 (2011).

[43] R. D. Shannon, Revised effective ionic radii and systematic studies of interatomic distances in halides and chalcogenides, Acta Crystallogr. **32**, 751 (1976).

[44] R. M. Badger, A relation between internuclear distances and bond force constants, J. Chem. Phys. **2**, 128 (2004).

[45] G. Petretto, S. Dwaraknath, H. P. C. Miranda, D. Winston, M. Giantomassi, M. J. van Setten, X. Gonze, G. Hautier, and G.-M. Rignanese, High-throughput density-functional perturbation theory phonons for inorganic materials, Sci. Data **5**, 180065 (2018).

[46] M. C. Oliveira, R. A. P. Ribeiro, E. Longo, M. R. D. Bomio, and S. R. de Lázaro, Quantum mechanical modeling of Zn-based spinel oxides: Assessing the structural, vibrational, and electronic properties, Int. J. Quantum Chem. **120**, e26368 (2020).

[47] M. Ceriotti, F. Pietrucci, and M. Bernasconi, *Ab Initio* study of the vibrational properties of crystalline TeO_2: The α, β, and γ phases, Phys. Rev. B **73**, 104304 (2006).

[48] L. Debbichi, M. C. Marco De Lucas, J. F. Pierson, and P. Krüger, Vibrational properties of CuO and Cu_4O_3 from first-principles calculations, and raman and infrared spectroscopy, J. Phys. Chem. C **116**, 10232 (2012).

[49] M. Khedidji, F. Saib, O. Mahroua, and M. Trari, The structural, electronic, magnetic, optical and vibrational properties of the delafossite $CuAlO_2$: DFT calculations and experimental study, J. Mater. Sci. Mater. Electron. **33**, 26474 (2022).

[50] A. P. Ayala, I. Guedes, E. N. Silva, M. S. Augsburger, M. Del, and J. C. Pedregosa, Raman investigation of A_2CoBO_6 (A = Sr and Ca, B = Te and W) double perovskites, J. Appl. Phys. **101**, 123511 (2007).

[51] S. C. Lal, J. Isuhak Naseemabeevi, and S. Ganesanpotti, Distortion induced structural characteristics of $Ba_2R_{2/3}TeO_6$ (R = Y, Gd, Tb, Dy, Ho, Er, Tm, Yb and Lu) double perovskites and their multifunctional optical properties for lighting and ratiometric temperature sensing, Mater. Adv. **2**, 1328 (2021).

[52] O. P. Missen, S. J. Mills, S. Canossa, J. Hadermann, G. Nénert, M. Weil, E. Libowitzky, R. M. Housley, W. Artner, A. R. Kampf, and M. S. Rumsey, Polytypism in mcalpineite: A study of natural and synthetic Cu_3TeO_6, Cryst. Eng. Mater. **78**, 20 (2022).

[53] E. B. Wilson, Some mathematical methods for the study of molecular vibrations, J. Chem. Phys. **9**, 76 (2004).

[54] J. Gaunt, The force constants and bond lengths of some inorganic hexafluorides, Trans. Faraday Soc. **50**, 546 (1954).

[55] J. Ruiz-Fuertes, D. Errandonea, S. López-Moreno, J. González, O. Gomis, R. Vilaplana, F. J. Manjón, A. Muñoz, P. Rodríguez-Hernández, A. Friedrich, I. A. Tupitsyna, and L. L. Nagornaya, High-pressure raman spectroscopy and lattice-dynamics calculations on scintillating $MgWO_4$: Comparison with isomorphic compounds, Phys. Rev. B **83**, 214112 (2011).

[56] M. N. Iliev, M. M. Gospodinov, and A. P. Litvinchuk, Raman spectroscopy of $MnWO_4$, Phys. Rev. B **80**, 212302 (2009).

[57] R. Lacomba-Perales, D. Errandonea, D. Martinez-Garcia, P. Rodríguez-Hernández, S. Radescu, A. Mujica, A. Muñoz, J. C. Chervin, and A. Polian, Phase transitions in wolframite-type $CdWO_4$ at high pressure studied by raman spectroscopy and density-functional theory, Phys. Rev. B **79**, 094105 (2009).

[58] Y. Liu, H. Wang, G. Chen, Y. D. Zhou, B. Y. Gu, and B. Q. Hu, Analysis of raman spectra of $ZnWO_4$ single crystals, J. Appl. Phys. **64**, 4651 (1988).

[59] S. S. Saleem, Infrared and raman spectroscopic studies of the polymorphic forms of nickel, cobalt and ferric molybdates, Infrared Phys. **27**, 309 (1987).

[60] P. Pramanik, S. Singh, M. R. Chowdhury, S. Ghosh, V. Sathe, K. M. Rabe, D. Vanderbilt, M. S. Seehra, and S. Thota, Lattice dynamics and magnetic exchange interactions in $GeCo_2O_4$: A spinel with pyrochlore lattice, Phys. Rev. B **104**, 014433 (2021).

[61] B. Rivas-Murias and V. Salgueiriño, Thermodynamic CoO–Co_3O_4 crossover using raman spectroscopy in magnetic octahedron-shaped nanocrystals, J. Raman Spectrosc. **48**, 837 (2017).